International Journal of Microwave and Wireless Technologies

cambridge.org/mrf

Linear dimensional lung phantoms for the microwave-based detection of acute respiratory distress syndrome

Laya Joseph[1], Martin Fabioux[2], Arvind Selvan Chezhian[3], Thiemo Voigt[3], Roger Karlsson[3] and Robin Augustine[4]

[1]Department of Electrical Engineering, Uppsala University, Uppsala, Sweden; [2]Department of Electrical Engineering, Ecole Supérieure d'Électronique de l'Ouest, Angers, France; [3]Networked Embedded Systems Division, Department of Electrical Engineering, Uppsala Universitet, Uppsala, Sweden and [4]Electrical Engineering, Uppsala Universitet, Uppsala, Sweden

Research Paper

Cite this article: Joseph L, Fabioux M, Selvan Chezhian A, Voigt T, Karlsson R, Augustine R (2025) Linear dimensional lung phantoms for the microwave-based detection of acute respiratory distress syndrome. *International Journal of Microwave and Wireless Technologies*, 1–10. https://doi.org/10.1017/S175907872500056X

Received: 22 February 2025
Revised: 15 March 2025
Accepted: 4 April 2025

Keywords:
ARDS; dielectric probe; dielectric properties; IFAC; linear dimensional lung phantoms; microwave radiation; numerical simulations; semisolid; *S*-parameters

Corresponding author: Robin Augustine; Email: robin.augustine@angstrom.uu.se

Abstract

Acute respiratory distress syndrome (ARDS) is a critical lung condition caused by trauma or infection. This study explores the development and evaluation of human lung phantoms to investigate the feasibility of using microwave frequencies for ARDS detection. Both physical semisolid phantoms and their numerical models were developed in inflated and deflated states to replicate the dielectric properties of healthy and affected lungs. Three phantom sets with varying water and air content were fabricated to simulate different stages of respiratory distress. The geometric parameters of the phantoms were derived from CT scans of 166 ARDS patients. Dielectric permittivity and conductivity were measured using a Keysight N1501A dielectric probe over a 0.5–13 GHz range, showing strong agreement with IFAC's reference data. To validate the models, horn antennas operating between 8.2–12.4 GHz were used to measure *S*-parameters (S11 and S21) in both physical and numerical phantoms. The results demonstrated consistent changes in transmission and reflection characteristics corresponding to variations in lung volume and dielectric properties. These findings support the potential of microwave imaging as a non-invasive tool for early ARDS detection by effectively distinguishing between healthy and distressed lung states based on measurable electromagnetic response.

Introduction

An earlier less extensive version of this paper was presented at the 18th European Conference of Antennas and Propagation (EuCAP) and published in its proceedings [1]. Acute respiratory distress syndrome (ARDS) is a pathological condition affecting lungs and causes fluid to leak into the alveoli, making it difficult to oxygenate the bloodstream. After COVID-19, several studies reported that hundreds of adults are affected by ARDS [2, 3]. This condition often arises as a complication of pneumonia associated with COVID-19. Studies [2, 4] also show that the major cause of death in COVID-19 is ARDS after the cytokine storm and frequent microvascular thrombotic events and multi-organ system failure.

Significant studies are ongoing in the research field to analyze the post-COVID lung respiratory distress. The early stages of respiratory syndrome in COVID-19 patients are not so easy to identify and, once identified, it is necessary to optimize patient follow-ups [5].

To diagnose and analyze the pathology in the lungs, chest X-rays and computer tomography (CT) image techniques are widely employed. During the course of patient treatments, it is observed that many CT and X-ray scans with a specific interval time have to be performed on patients until their full recovery. Pan et al. [4] describe the chest CT findings associated with COVID-19 pneumonia from initial diagnosis until patient recovery. They found that a total of 82 pulmonary CT scans had been performed within a range of 1–8 days with a mean interval of 4 ± 1 days on 21 patients. This shows that the identification of ARDS from the initial stage to patient recovery is a complex and time-consuming procedure and the patients have to go through multiple clinical tests.

Tissue emulatory models (TEMs), or phantoms, are becoming increasingly valuable in biological and medical applications for validating and testing precursor systems. These phantoms are constructed from artificial materials designed to mimic the physical and dielectric properties of real human tissues [6]. TEMs can be employed in the biomedical field for early disease detection through testing and evaluating the performance and safety of microwave-based medical devices, reducing electromagnetic (EM) interaction with the patient's body. To effectively replace human tissues or organs, TEMs must exhibit specific characteristics, including physical and structural realism, dielectric precision, and durability for repeated tests and measurements.

Patients with ARDS develop pulmonary edema, where fluid leakage into the pulmonary parenchyma floods the alveolar spaces [7]. The alveoli flooding increases lung water content [8], and some studies show a rise of 75–100% compared to normal levels [9]. Additionally, studies [10, 11] indicate that the lung volume decreases in ARDS patients.

Wireless communication through the human body depends on several factors, including water content, conductivity, thickness, and volume of the tissues and organs in the body. There is a direct correlation between the water content and the dielectric properties of the biological tissues [12]. An increase in lung water content and changes in lung volume alter the dielectric permittivity of lung tissues.

Several methods have been developed to detect infiltrated lung water, including chest radiograph, CT, magnetic resonance imaging, positron emission tomography, external radio flux detection, and the soluble gas method [13]. Microwave-based techniques are widely used in medical diagnosis, disease treatment, and patient monitoring due to its non-ionizing nature and low cost [14–17]. With microwaves, changes in the amplitude of the S-parameters can be measured to detect variations in the dielectric permittivity of the targeted materials. Since 1973, microwave technology has been employed to detect lung diseases, with numerous studies developed by transmitting microwave signals through the lungs and observing variations in the reflection and transmission coefficients [18–20]. The microwave technique can be considered convenient due to its portability, low cost, and noninvasive nature.

Aim of the work

We aim to create artificial lung models as test beds for microwave techniques, a noninvasive and real-time approach, which potentially enables earlier detection, continuous monitoring, and personalized treatment of ARDS. The overarching aims of this work are to (1) design models of healthy, deflated, and inflated human lung lobes, to account their linear dimensional parameters; (2) develop TEMs and their numerical models for both the left and right lung lobes, including healthy, inflated, and deflated models, as well as three sets of diseased, inflated, and deflated lung TEMs with infiltrated water leakage, representing different stages of ARDS; and (3) validate the applicability of these lung phantoms. Validation is conducted by analyzing and comparing the impact of lung conditions through laboratory measurements and numerical simulations of reflection (S_{11}) and transmission (S_{21}) parameters using horn antennas at microwave frequencies.

Outline of the work

In section "Methodology" of this paper, the details of data collection, the design of left and right lobes of both deflated and inflated human lungs, the materials used for healthy and diseased TEMs, and the fabrication procedures are outlined. In section "Results and discussions," we present and discuss the dielectric measurement results of the developed lung TEMs across the 0.5–13 GHz frequency range, comparing with the reference IFAC database. Section "Results and discussions" also addresses the applicability of the TEMs by measuring and simulating the S_{11} and S_{21} parameters on physical and numerical phantom models. In section "Conclusion," we summarize the study and discuss the results.

Methodology

Materials

Our goal was to fabricate semisolid lung TEMs that emulate the physical, structural, and dielectric properties of real human lungs. The semisolid consistency allows the phantom mixture, initially in a viscous liquid form, to be cast into 3D-printed lung molds, effectively mimicking realistic soft lung tissue. The dielectric properties of both healthy and diseased, inflated and deflated lung tissues vary with the water content, ranging from low to high values. The material selection for the lung TEMs is based on the semisolid phantoms [6, 21–23]. We propose novel recipes with new material compositions for both healthy and diseased lung TEMs. The materials include deionized (DI) water, glycerine, corn flour, gelatine, dextrin, canola oil, TX-151, surfactant, sodium chloride (NaCl), and sodium benzoate. Different materials and ingredient proportions were used to modify the dielectric properties of the healthy and diseased TEMs. The material composition for healthy and diseased (three stages of ARDS), inflated and deflated lung phantoms is shown in Table 1, with the materials listed by their weight percentages.

The primary use case of the TEMs is diagnosing ARDS, which is fundamentally caused by fluid (primarily water) accumulation in the lungs. This condition can be classified into different levels based on the amount of water lodged in the alveoli. The hypothesis is that variations in dielectric properties arise from changes in the water and air content in the lungs compared to the baseline dielectric value of lung tissue. In the inflated state, the dielectric property of the lungs can be approximated using Maxwell's mixture equation, accounting for the volume of air trapped in the lungs, the volume of lung tissue, and their respective dielectric values. In contrast, in the deflated state, the effective relative permittivity is equivalent to that of the lung tissue alone, as less air is present.

DI water is the primary solvent in the materials, and the relative permittivity is directly proportional to the water content. Due to the distribution of water and air, the relative permittivity is lower in inflated lungs compared to deflated lungs. To emulate this condition, the deflated lung phantoms were fabricated with a higher water content (by adding DI water) along with adjustments in other ingredient proportions. We modeled each set of diseased inflated and deflated lung phantoms with approximately 40–50% increase in water content compared to healthy inflated and deflated ones. As water content in the lung tissues increases with the progression of ARDS, we used approximately 11%, 19%, and 32% more water content in the three stages of inflated ARDS lung phantoms compared to the healthy inflated lung phantom. Similarly, we used 17%, 21%, and 27% more water content in the three successive stages of ARDS deflated lung phantoms compared to the healthy deflated lung phantom. The amount of DI water required to adjust the dielectric properties of each recipe varies depending on the estimated difference in dielectric properties and is not directly proportional to the total water content in the lungs. The exact percentage of water used for the inflated and deflated lung scenarios differs, as they are based on two distinct recipes.

Glycerine is another solvent but with lower dielectric permittivity compared to DI water. Gelatine and TX-151 (a super-stuff agent) provide the semisolid consistency to the lung TEMs. Canola oil with low dielectric permittivity is used in the deflated lung phantoms to achieve lower relative permittivity. Corn flour and dextrin bind the various materials together and help regulate the dielectric properties. A surfactant (dish washing liquid) is used as

Table 1. Material composition for healthy and diseased ARDS inflated and deflated lung phantoms. Values in weight %

Materials	Inflated lung				Deflated lung			
	Healthy	Diseased 1	Diseased 2	Diseased 3	Healthy	Diseased 1	Diseased 2	Diseased 3
DI water	41.5	46	49.2	54.6	60	70	72.5	76
Gelatine	5.5	5.1	6.2	—	9.4	7	7.3	5.6
Glycerine	12.4	11.4	11	—	14	10.5	7.3	8.4
Dextrin	—	—	—	—	16.4	12.3	12.7	9.8
Corn flour	24.9	23	22.1	29.2	—	—	—	—
Canola oil	13.9	12.8	9.8	9.8	—	—	—	—
Surfactant	1.4	1.3	1.3	0.9	—	—	—	—
Sodium benzoate	0.4	0.4	0.4	0.4	0.2	0.2	0.2	0.2
TX-151	—	—	—	4.9	—	—	—	—
Salt	—	—	—	0.2	—	—	—	—

Table 2. Extracted linear dimensions and volume with standard deviation of the left-hand side and right-hand side inflated lungs [25]

Linear dimensions	Lungs	Data
Peak-to-peak	—	8.3 ± 1.2 cm
Height	Right	20.6 ± 2.6 cm
	Left	19.8 ± 2.6 cm
Maximum height	Right	26.9 ± 2.7 cm
	Left	26.1 ± 2.6 cm
Width	Right	11.6 ± 1.2 cm
	Left	10.0 ± 1.0 cm
Depth	Right	16.9 ± 1.8 cm
	Left	17.1 ± 2.0 cm
Volume	Right	2663 ± 667 cm^3
	Left	2301 ± 636 cm^3

an emulsifier to dissolve oil droplets in the phantoms. NaCl regulates conductivity in the phantom, while sodium benzoate (food preservative) is added to extend the shelf life of the lung phantoms.

Data collection for the design of lung TEMs

To mimic the exact size, shape, and volume of the inflated lungs, we have used CT studies of air and tissue distribution in the lungs of healthy volunteers and of patients with ARDS [24] and a collaboration work done between the Human Monitoring Laboratory (HML) and the Montreal University Hospital Centre (CHUM) [25]. We extracted the linear dimensions and volumes of lungs, as calculated from CT images from 166 patients [25]. These data were collected while the patients had taken a deep breath prior to the imaging and their lungs were larger than the usual at-rest volume. The data are based on the study on both males and females to find out linear dimensions with respect to age, height, and weight. The study shows that linear dimensions of lungs are essentially independent of age, height, and weight. Table 2 shows the extracted linear dimensions and volume with standard deviation of the left and right lungs [25]. We have chosen the combined data sets of females and males for our TEM design. Uneri et al. [26] analyzed the physical and topological properties during surface deformation of deflated lung using mesh models for both inflated and deflated states. The analysis reveals that a substantial linear deformation of 20% is present in deflated lungs compared to that of inflated lungs [25]. Therefore, we have chosen the deflated lung dimensions by reducing 20% of the inflated lungs.

Design of healthy inflated and deflated lung TEM molds

The 3D-printed molds for both the inflated and deflated TEMs were designed based on the data provided in section “Data collection for the design of lung TEMs,” enabling the liquid phantom mixture to be cast after fabrication. SOLIDWORKS design software was used to create the CAD model for the lung molds. Polylactic acid was selected as 3D printing material for the pulmonary molds due to its heat tolerance and cost-effectiveness. Figure 1 shows the 3D-printed molds, with (a) the inflated lung mold with the trachea and (b) the deflated lung molds. As illustrated, the dimensions and volume of the inflated lung molds are larger than those of the deflated lung molds.

Fabrication of lung TEMs

The fabrication of inflated and deflated sets of healthy and diseased lung TEMs was carried out in a solvent fume hood in a clean room environment. We developed novel fabrication procedures to accurately mimic the physical and dielectric properties such as relative permittivity (ε_r) and loss tangent (tan δ) for the lung TEMs over the 0.5–13 GHz frequency range. Considering both the deflated and inflated models of healthy lungs and three stages of ARDS lungs, there is a significant difference in relative permittivity among the lungs. We selected different materials, ingredient compositions, and fabrication procedures to model the lungs from higher to lower permittivity.

The Institute for Applied Physics “Nello Carrara” (IFAC) in Florence, Italy, has reported extrapolated complex permittivity values of human tissues up to 110 GHz [27]. Several iterations of material compositions were tested to match the values reported in the IFAC data base. A double boiling technique was employed to combine water with gelatine and TX-15, with the temperature regulated around 90°C to ensure the cross-linking of gelatine and water molecules. During each phase of the fabrication process, the

https://doi.org/10.1017/S175907872500056X Published online by Cambridge University Press

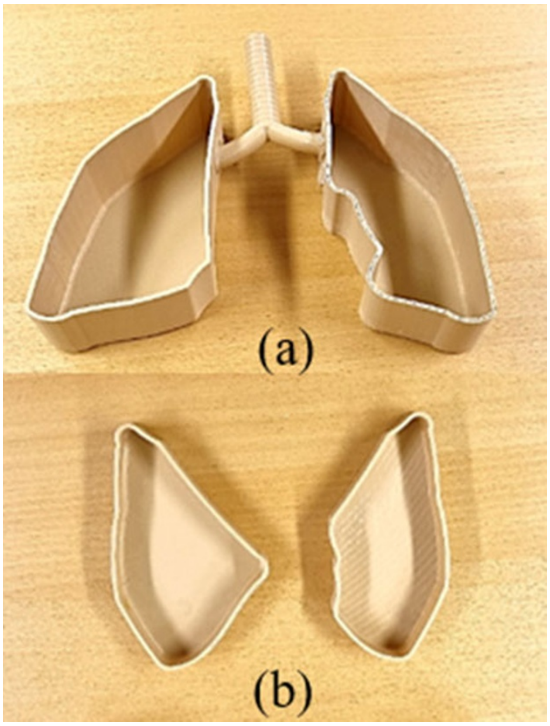

Figure 1. 3D-printed (a) inflated lung molds with trachea and (b) deflated lung molds.

phantom mixture was stirred continuously to maintain homogeneity. The final viscous mixture was cooled in a cold-water bath before being poured into the 3D-printed molds. The lung phantoms were then left at room temperature to solidify, and then the TEMs were properly wrapped in saran wrap (polyethylene food wrap). Once the TEMs had jellified in the molds, they were carefully separated and stored in a refrigerator. The TEMs should be removed from the refrigerator and kept in room temperature before measurements are taken.

Measurement methods

We employed two different measurement techniques for evaluating the fabricated lung TEMs. The first involved using an open-ended coaxial transmission line technique with a Keysight slim-form probe kit [28] and a FieldFox N9918A network analyzer for dielectric characterization [29]. This technique incorporates Debye and Maxwell models, alongside the single-pole Cole–Cole equation, to detect changes in the relative permittivity and conductivity of the lung TEMs due to variations in water content. The relative permittivity and loss tangent were measured across the 0.5–13 GHz frequency range. These nondestructive, real-time measurements were obtained by immersing the slim probe approximately 2–3 mm deep into the lung tissue phantom. To ensure homogeneity in both the inflated and deflated TEMs, four random measurements with 801 linearly spaced frequency points were taken at different positions on each lung TEM, and the mean value of these measurements was compared with the IFAC database. Figure 2(a) illustrates the dielectric measurement characterization of the lung phantoms.

To validate the applicability of the fabricated lung phantoms, we conducted laboratory measurements and numerical simulations. In the laboratory evaluation, we measured the S_{11} and S_{21} parameters using 15 dBi standard gain horn antennas (PEWAN090-15SF), designed for the 8.2–12.4 GHz frequency range and a Keysight FieldFox network analyzer (N9918A). These horn antennas were chosen for small size making them convenient for a bench top experiments and furthermore our phantoms cover the antenna's operational frequencies. First, the transmitter and receiver antennas were connected to ports 1 and 2 of the FieldFox, respectively, and free-space measurements were taken by placing the antennas facing each other with their apertures 19 cm apart. The spacing between the antennas was fixed at 19 cm for all measurements in order to provide at least a 2.5 cm gap between inflated phantom (largest phantom dimension, 14 cm across) and the antenna apertures.

Next, the S_{11} and S_{21} parameters were measured by positioning the healthy inflated lung phantom between the transmitter and receiver antennas, maintaining the same 19 cm distance between the two antennas, with the phantom equidistant (2.5 cm) from both. Variations were observed in the reflection and transmission parameters due to differences in the phantoms' dielectric properties, size, and thickness. The process was repeated with the healthy deflated lung phantom (7 cm across) with a gap of 6 cm on both sides. Figure 2(b) and (c) shows the S-parameter measurement setup with the deflated and inflated lung phantom.

The numerical study involves S-parameter simulations of the numerical models – both inflated and deflated – using CST Studio Suite software. These numerical models replicate the size, shape, and volume of the physical lung phantoms and the horn antennas. To analyze the feasibility of using lung TEMs in comparison with the real-life scenarios in humans, the inflated and deflated numerical models were designed to emulate the dielectric properties from the IFAC database [27]. The validation of the lung TEMs were performed by comparing the results obtained from the measurements with the numerical simulations. Figure 3(a) and (b) depicts the CST S-parameter simulation setups of the inflated and deflated models, respectively.

Results and discussions

A set of linear dimensional inflated and deflated lung phantoms were designed and fabricated to emulate healthy human lungs. Additionally, three sets of inflated and deflated diseased lung phantoms were developed to represent three stages of ARDS, characterized by increased water leakage into the alveoli of lung tissues. For the design of the left and right lobes of the inflated and deflated healthy lungs, we considered key linear dimensions such as height, width, depth, and lung volume. All the lung TEMs were fabricated with a semisolid consistency to mimic the soft tissue of the lungs and achieve dielectric precision across the 0.5–13 GHz frequency range. Figure 4(a) illustrates the fabricated left and right lobes of the healthy deflated lung TEM, and (b) the left lobes of the healthy inflated and deflated lung TEMs and their respective mold designs. Figure 4(b) highlights the difference in size between the inflated and deflated left lung lobes.

The evaluation of the fabricated lung TEMs, including both healthy and diseased models, was conducted by performing dielectric characterization across the 0.5–13 GHz frequency range. Table 3 presents the relative permittivity and loss tangent values at 2.45 GHz for all left and right lung TEMs, alongside the

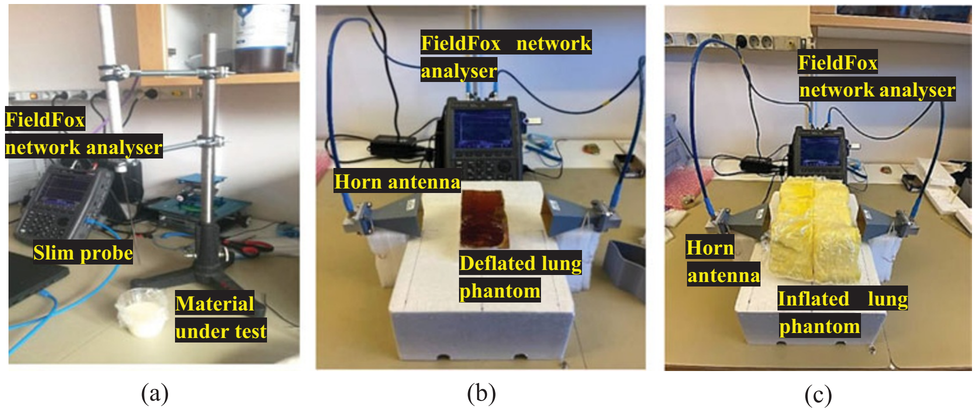

Figure 2. (a) Setup for dielectric characterization of a lung sample, (b) *S*-parameter measurements of deflated, and (c) inflated lung phantoms.

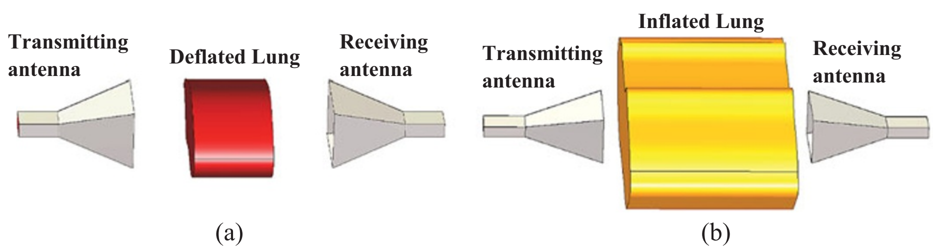

Figure 3. CST simulation setups of (a) deflated lung and (b) inflated lung.

Figure 4. (a) Fabricated left and right lobes of healthy deflated lung TEMs and (b) molds together with inflated and deflated left lobes of healthy lung TEMs.

Table 3. Relative permittivity and loss tangent at 2.45 GHz of inflated and deflated lungs and IFAC reference data of the left and right lungs

	Inflated		Deflated	
Lung types	Relative permittivity	Loss tangent	Relative permittivity	Loss tangent
IFAC	20.5	0.29	48.5	0.25
Healthy	20	0.38	48.1	0.33
Diseased 1	25.1	0.356	56.5	0.268
Diseased 2	30.2	0.359	59.8	0.247
Diseased 3	36.1	0.309	64.4	0.221

IFAC database values. The dielectric values of the lung TEMs agree well with the IFAC reference values. A comparison of the dielectric properties of the IFAC database and inflated and deflated healthy and diseased lungs across the 0.5–13 GHz frequency range is depicted in Figure 5. The graphs indicate that the relative permittivity and loss tangent of the healthy inflated and deflated lungs match the IFAC reference values over the entire frequency range. Additionally, the relative permittivity of the diseased, inflated lung in stage 3 shows higher values across the frequency range. It was observed that the relative permittivity of the inflated diseased stage 2 lung phantom overlaps with that of healthy at higher frequencies (from 6 GHz). The diseased stage 1 of inflated phantoms' relative permittivity overlaps the IFAC values at frequencies above 5.8 GHz. For the deflated lung phantoms, the

https://doi.org/10.1017/S175907872500056X Published online by Cambridge University Press

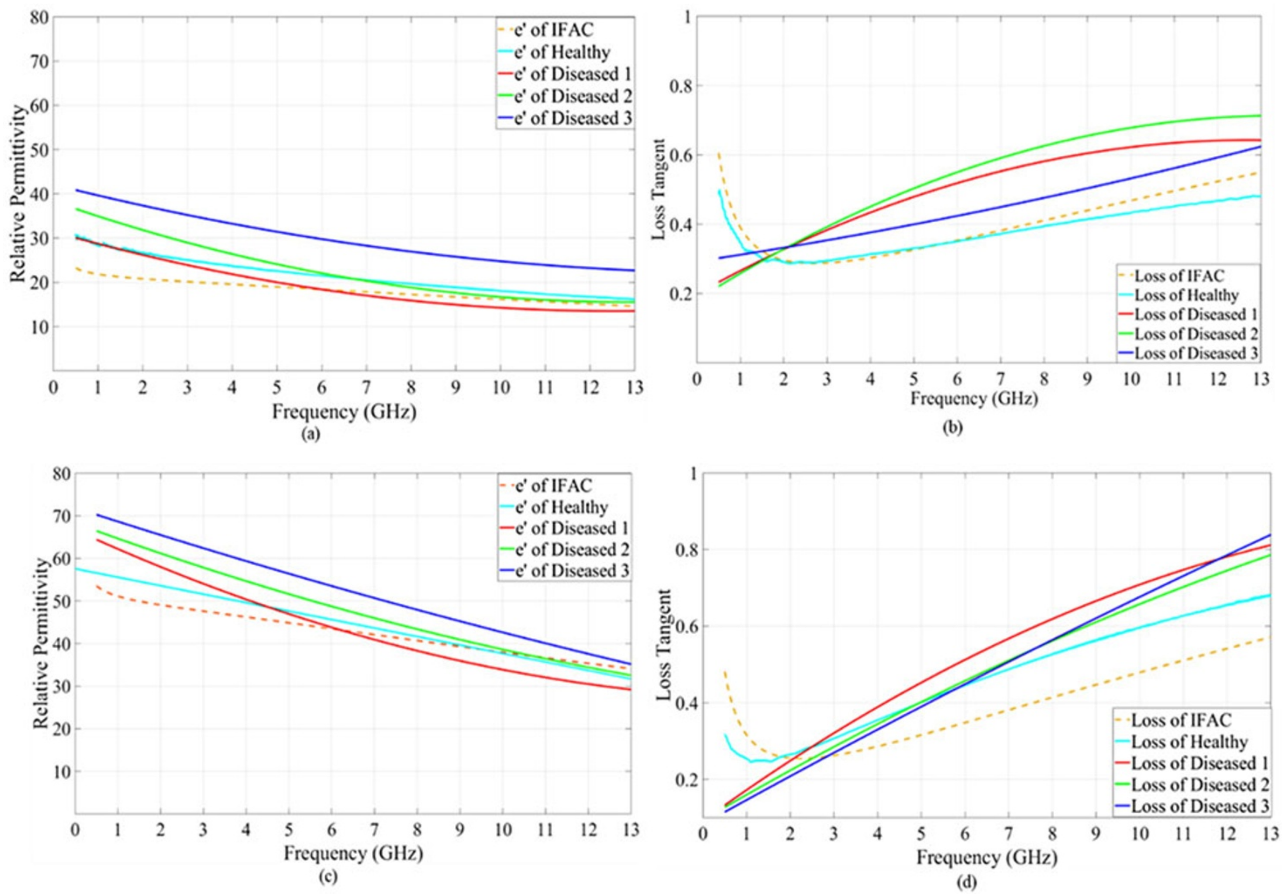

Figure 5. Dielectric properties of the IFAC database and measured with the dielectric probe, for inflated lung TEMs (a) and (b) and deflated lung TEMs (c) and (d).

relative permittivity of the stages 2 and 3 consistently shows higher values across the lower frequencies, while the relative permittivity of the stage 1 phantom overlaps with the IFAC values around 6 GHz.

The applicability of the fabricated inflated and deflated healthy lung phantoms was evaluated by comparing the measurement and the numerical simulations over the operating frequency range of the horn antennas, 8.2–12.4 GHz. Figure 6 presents the measured S_{11} and S_{21} parameters of the inflated and deflated healthy lungs along with free-space measurements over 7–13 GHz frequency range and Figure 7 shows the corresponding numerical simulation values.

For the free-space case, the S_{11} plots from both measurements and numerical simulations show minimal reflection values, while the S_{21} plots display high transmission values. When the inflated and deflated lungs were placed between the antennas, the reflection values (S_{11}) increased compared to the free-space case for both measurements and simulations. The transmission values (S_{21}) for the free-space measurement and simulation show higher values than for the inflated and deflated lung TEMs, indicating small transmission losses in air. The simulated transmission (S_{21}) values for the inflated lung are lower than those from the measurements, likely due to the differences in dielectric properties assigned to the numerical models, as per the IFAC database. The deflated phantom, which has relatively low loss ($\tan\delta = 0.33$) and lower thickness has higher transmission (S_{21}) values compared to the inflated phantom, which is thicker and has a higher loss ($\tan\delta = 0.38$). Similarly, the simulated deflated model has higher transmission values (S_{21}) values than the deflated model.

Table 4 presents the measured and simulated S_{11} and S_{21} values of the healthy inflated and deflated lung models, along with the corresponding free-space values at the horn antenna centre frequency of 10 GHz. A strong correlation of S_{21} values can be seen for the inflated and deflated cases where a high loss tangent results in a significant path loss. The inflated phantom (14 cm across) exhibits a higher path loss of 59 dB compared to the deflated phantom (7 cm across, 29 dB), indicating a trend in increased loss for larger lung dimensions. Similarly, the inflated numerical model has a higher path loss of 78 dB compared to the deflated numerical model (41 dB). The measured reflection, S_{11}, is higher for the inflated case (−7 dB) than for the deflated case (−12 dB). Also, the inflated numerical model shows a higher S_{11} of −7 dB compared to −8 dB for the deflated model. This difference is caused by a fixed spacing between the transmitter and receiver antennas of 19 cm, while the distance between the antenna aperture and the lung models' surfaces (both physical phantom and numerical models) varies with their size. For the inflated models, this distance is 2.5 cm, compared to 6 cm for the deflated models. Consequently, the reflections from the inflated models are higher due to its proximity to the horn antenna. The amplitude for the measured and numerically simulated S-parameters vary clearly between the inflated and deflated healthy models, which differ in thickness, relative permittivity, and loss tangent. This study confirms that microwave techniques can effectively detect variations in lung

https://doi.org/10.1017/S175907872500056X Published online by Cambridge University Press

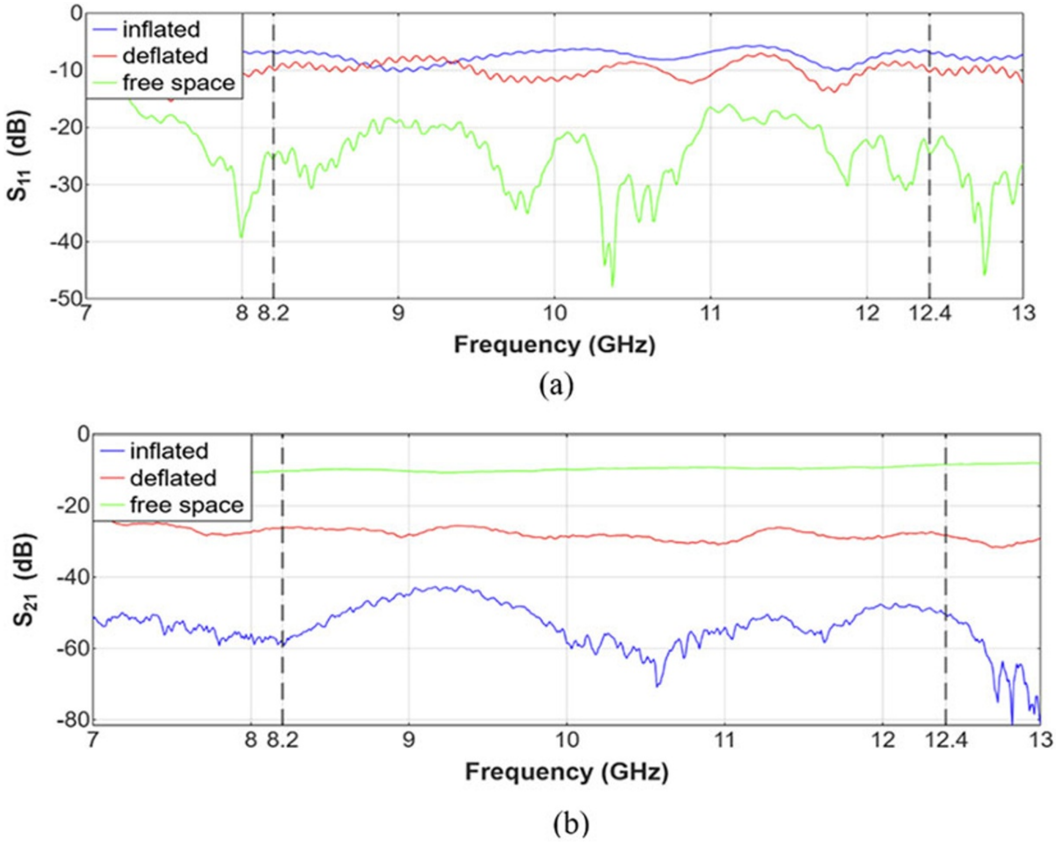

Figure 6. Measured (a) reflection (S_{11}) and (b) transmission (S_{21}) coefficients of inflated and deflated healthy lung phantoms and free-space.

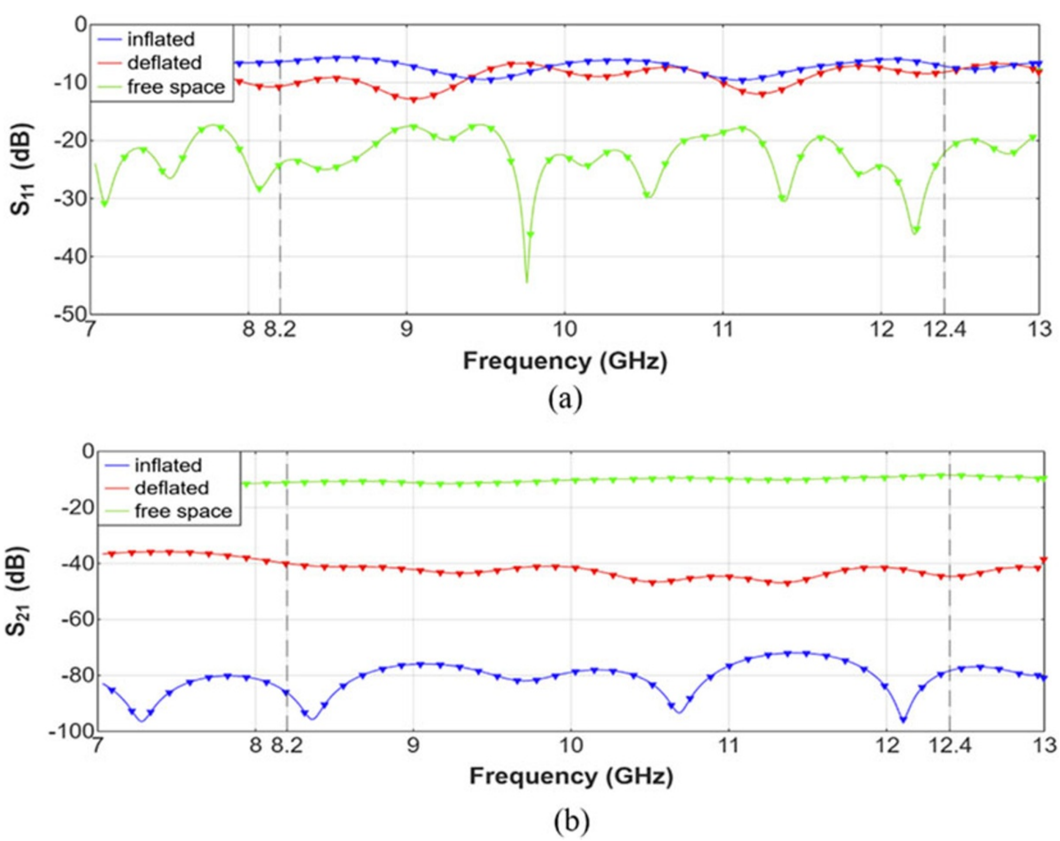

Figure 7. Simulated (a) reflection ($S11$) and (b) transmission ($S21$) coefficients of inflated and deflated healthy lung numerical models and free-space.

https://doi.org/10.1017/S175907872500056X Published online by Cambridge University Press

Table 4. Reflection and transmission parameters of free-space, healthy inflated and deflated lung phantoms at 10 GHz

S-parameters	Free space (dB)	Inflated lung (dB)	Deflated lung (dB)
S_{11} (measured)	−23	−7	−12
S_{11} (simulated)	−22	−7	−8
S_{21} (measured)	−10	−59	−29
S_{21} (simulated)	−10	−78	−41

condition with respect to the increased water content and higher relative permittivity by measuring transmission and reflection coefficients. As discussed in the introduction, the lung volume decreases in ARDS patients, and our *S*-parameter measurement and simulation results show amplitude changes corresponding to these lung volume reductions, as well.

The present study was conducted with phantom and numerical models placed in free space. For more realistic future measurements and simulations, the lung models can be placed within an elaborate thoracic cavity model.

When we compare the numerical simulations with measurement results, it can be seen that the S_{11} and S_{21} values are generally similar. The measured S_{21} shows a higher amplitude compared to the simulated S_{21} and this could be attributed to the surface coupling facilitated in the measurement whereas the boundary conditions assigned in simulation mitigates it and provides a signal path through the phantom which offers a lower amplitude in S_{21}. This signifies further importance of coupling medium in physical measurements. The correlation of the measurement and numerical results shows that our lung phantoms are performing well with respect to IFAC lung models used in the simulations.

Conclusion

A set of linear dimensional, semisolid healthy, deflated, and inflated lung phantoms, along with three stages of diseased, inflated, and deflated lung tissue phantoms, were fabricated. All phantoms were designed to emulate the physical and dielectric properties of human lung tissues. The design data for healthy deflated and inflated lungs were derived from a study of CT images from 166 patients. Corresponding lung phantom molds were 3D-printed. Key linear dimensions, such as height, width, depth, and volume, were considered in the design process.

The fabricated healthy and diseased lung phantoms were validated through dielectric measurements, including relative permittivity and loss tangent over the 0.5–13 GHz frequency range, which showed good agreement with the reference IFAC database. Numerical models replicating the deflated and inflated phantoms were developed with identical linear dimensions and dielectric values from the IFAC database. The applicability of these healthy lung phantoms was further evaluated and validated by measuring the S_{11} and S_{21} parameters using a standard gain horn antenna over the 7–13 GHz frequency range and comparing them with the simulated *S*-parameters of the numerical lung models. The results indicate that changes in dielectric properties, thickness, and volume can be detected by transmitting microwave signals through the lung phantoms, demonstrating the viability of microwave technology in detecting ARDS due to water leakage into lung tissue.

Funding statement. The authors thank the funding assistance from the Swedish Research Council (VR) project MuSkeldiagnosis (2023-03457) and the Swedish Foundation for Strategic Research (SSF) project Zero_IoT (210101-261231).

Competing interests. The authors declare no competing interest.

References

1. **Joseph L, Chezhian AS, Voigt T, Perez MD and Augustine R** (2024) Development of tissue emulatory models/phantoms of lungs at microwave frequency for acute respiratory distress syndrome. In *18th European Conference on Antennas and Propagation (EuCAP 2024)*, Glasgow, United Kingdom, 1–5.
2. **WHO COVID-19 Situation Report**, Coronavirus disease (COVID-19) epidemiological updates and monthly operational updates. https://www.who.int/emergencies/diseases/novel-coronavirus-2019/situation-reports (accessed 12 March 2025).
3. **Molina-Molina M and Hernández-Argudo M** (2022) Respiratory consequences after COVID-19: Outcome and treatment. *Revista Española de Quimioterapia* **35**(1), 67–72.
4. **Pan F, Ye T, Sun P, Gui S, Liang B, Li L, Zheng D, Wang J, Hesketh RL, Yang L and Zheng C** (2020) Time course of lung changes at chest CT during recovery from coronavirus disease 2019 (COVID-19). *Radiology* **295**(3), 715–721.
5. **Molina-Molina M, Valenzuela C, Ríos-Cortés A, ArbillagaEtxarri A, Torralba Y, Diaz-Perez D, Landete P, Mediano O, Tomás L, Rodriguez Pascual L, Jara-Palomares L, López-Reyes R and de la Rosa D** (2020) Spanish Society of Pulmonology and Thoracic Surgery (SEPAR) consensus for post-COVID-19 clinical follow-up. *Open Respiratory Archives* **2**, 278–283.
6. **Mobashsher AT and Abbosh AM** (2015) Artificial human phantoms: Human proxy in testing microwave apparatuses that have electromagnetic interaction with the human body. *IEEE Microwave Magazine* **16**(6), 44–62.
7. **Gonzales JN, Lucas R and Verin AD** (2015) The acute respiratory distress syndrome: Mechanisms and perspective therapeutic approaches. *Austin Journal of Vascular Medicine* **2**(1), 1009.
8. **Bongard FS, Matthay M, Mackersie RC and Lewis FR** (1984) Morphologic and physiologic correlates of increased extravascular lung water. *Surgery* **96**, 395–403.
9. **Sibbald WJ, Warshawski FJ, Short AK, Harris J, Lefcoe MS and Holliday RL** (1983) Clinical studies of measuring extravascular lung water by the thermal dye technique in critically ill patients. *Chest* **83**(5), 725–731.
10. **Gattinoni L, Tonetti T and Quintel M** (2017) Regional physiology of ARDS. *Journal of Critical Care* **21**(3), 312.
11. **Aguirre-Bermeo H, Turella M and Bitondo M** (2018) Lung volumes and lung volume recruitment in ARDS: A comparison between supine and prone position. *Annals Journal of Intensive Care* **8**, 25.
12. **Di Meo S, Bonello J, Farhat I, Farrugia L, Pasian M, Camilleri Podesta MT, Suleiman S, Calleja-Agius J and Sammut CV** (2022) The variability of dielectric permittivity of biological tissues with water content. *Journal of Electromagnetic Waves and Applications* **36**(1), 48–68.
13. **Staub NC** (1986) Clinical use of lung water measurements: Report of workshop. *Chest* **90**(4), 588–594.
14. **Lui HS and Persson M** (2024) Microwave and antenna systems in medical applications. *IEEE Sensors* **24**, 1059.
15. **Chandra R, Zhou H, Balasingham I and Narayanan RM** (2015) On the opportunities and challenges in microwave medical sensing and imaging. *IEEE Transactions on Biomedical Engineering* **62**, 1667–1682.
16. **Chiao JC, Changzhi L, Jenshan L, Caverly RH, Hwang JCM, Rosen H and Arye R** (2022) Applications of microwaves in medicine. *IEEE Journal of Microwaves* **3**, 134–169.
17. **Joseph L, Asan NB, Ebrahimizadeh J, Chezhian AS, Perez MD, Voigt T and Augustine R** (2020) Non-invasive transmission based tumor detection using anthropomorphic breast phantom at 2.45 GHz. *In14th European*

Conference on Antennas and Propagation (EuCAP, 2020), Copenhagen, Denmark.
18. **Susskind C** (1973) Possible use of microwaves in the management of lung disease. *Proceedings of the IEEE* **61**, 673–674.
19. **Gagarin R, Celik N, Youn HS and Iskander MF** (2011) Microwave stethoscope: A new method for measuring human vital signs. In *IEEE International Symposium on Antennas and Propagation (APSURSI 2011).*
20. **Celik N, Gagarin R, Huang GC, Iskander MF and Berg BW** (2013) Microwave stethoscope: Development and benchmarking of a vital signs sensor using computer-controlled phantoms and human studies. *IEEE Transactions on Biomedical Engineering* **61**, 2341–2349.
21. **Joseph L, Perez MD and Augustine R** (2019) Development of 500 MHz–20 GHz ultra-wideband multi-layered heterogeneous phantom of different human soft tissues for various microwaves based biomedical applications. In *13th European Conference on Antennas and Propagation (EUCAP 2019*), Krakow, Poland.
22. **Joseph L, Asan NB, Ebrahimizadeh J, Chezhian AS, Perez MD, Voigt T and Augustine R** (2020) Non-invasive transmission based tumor detection using anthropomorphic breast phantom at 2.45 GHz. In *14th European Conference on Antennas and Propagation (EuCAP 2020*), Copenhagen, Netherlands.
23. **Joseph L** (2019) Development of ultra-wide band 500 MHz–20 GHz heterogeneous multi-layered phantom comprises of human skin, fat and muscle tissues for various microwaves based biomedical application. Master's Thesis, Uppsala University
24. **Puybasset L, Cluzel P, Gusman P, Grenier P, Preteux F and Rouby JJ** (2000) Regional distribution of gas and tissue in acute respiratory distress syndrome. I. Consequences for lung morphology. *CT Scan ARDS Study Group. Intensive Care Medicine* **26**(7), 857–869.
25. **Kramer GH, Capello K, Bearss B, Lauzon A and Normandeau L** (2012) Linear dimensions and volumes of human lungs obtained from CT images. *Health Physics* **102**(4), 378–383.
26. **Uneri A, Nithiananthan S, Schafer S, Otake Y, Stayman JW, Kleinszig G, Sussman MS, Prince JL and Siewerdsen JH** (2013) Deformable registration of the inflated and deflated lung in cone-beam CT-guided thoracic surgery: Initial investigation of a combined model- and image-driven approach. *Medical Physics* **40**(1).
27. **Andreuccetti D, Fossi R and Petrucci C** (1997) An internet resource for the calculation of the dielectric properties of body tissues in the frequency range 10 Hz–100 GHz. Florence (Italy): IFAC-CNR.
28. **Keysight Technologies**, N1501A Dielectric Probe Kit 10 MHz to 50 GHz. Keysight.com. [Online]. Available at https://www.keysight.com/zz/en/assets/7018-04631/technical-overviews/5992-0264.pdf (accessed October 2023).
29. **Keysight Technologies**, FieldFox Handheld Analyzers: 4/6.5/9/14/18/26.5/32/44/50 GHz. Keysight.com. [Online]. Available at https://www.keysight.com/zz/en/assets/7018-03314/data-sheets/5990-9783.pdf (accessed October 2023).

Laya Joseph received the Engineering degree in Electronics and Communication from Calicut University, India, in 2009, and the master's degree in Engineering Physics from Uppsala University, Sweden, in 2019. She is currently doing her Ph.D. in Microwaves in Medical Engineering Group (MMG), Division of Solid-State Electronics, Department of Electrical Engineering, Angstrom Laboratoriet, Uppsala Universitet (UU), Sweden. She has worked as Research Engineer with the Microstructure Technology (MST), Material Science Department in 2020. Also, she has worked as research engineer the Angstrom Laboratory, Solid-State Electronics Division, Microwaves in Medical Engineering Group (MMG), Uppsala University, from 2019 to 2021. Her research interests include biological microwave phantoms for intrabody communication, fat intrabody communication, breast tumor sensing, and stretchable printed circuit boards for skin worn wireless networks.

Martin Fabioux is a student-engineer preparing a master's degree at the Ecole Supérieure d'Électronique de l'Ouest (ESEO) in Angers, working mainly in IT and electronics. He specializes in electronics and connected objects. He is currently doing a technical internship in Microwaves in Medical Engineering Group (MMG), at the Solid-State Electronics Division, Department of Electrical Engineering, Uppsala University, on human phantom models.

Arvind Selvan Chezhian is a Ph.D. student specializing in medical robotics and bio-mechatronics at the Department of Electrical Engineering, Solid-State Electronics, Uppsala University. His primary research focuses on 3D printing for biomedical applications, where he creates advanced prototypes of biomechatronic systems such as bionic arms and exoskeletons for medical robotics technologies. Arvind's work involves phantom fabrication for in-body communication (IBC), modeling complex tissues such as fat, muscle, skin, and bone to replicate human body structures in medical research. In addition to his core focus, he conducts microwave sensor testing and PCB fabrication. His interdisciplinary approach allows him to explore cutting-edge technologies to enhance mobility, rehabilitation, and prosthetic solutions. Arvind seeks to integrate these technologies seamlessly into the human body, ultimately improving patient care and quality of life. His innovative research positions him as a promising contributor to developing the next generation of biomedical devices, which aim to transform health-care and rehabilitation practices.

Thiemo Voigt (Member, IEEE) received the Ph.D. degree from Uppsala University, Sweden, in 2002. He is currently a Professor of Computer Science with the Department of Information Technology, Uppsala University. He also leads the Networked Embedded Systems Group, RISE Computer Science. His work has been cited more than 18,700 times. His current research interests include system software for embedded networked devices and the Internet of things. He is a member of the editorial board for the IEEE Internet of Things and ACM Transactions on Sensor Networks (TOSN).

https://doi.org/10.1017/S175907872500056X Published online by Cambridge University Press

Roger L. Karlsson received the M.Sc. degree in applied physics and the Ph.D. degree in space physics from Uppsala University, Uppsala, Sweden, in 1997 and 2005, respectively. In 2000, he cofounded the company Red Snake Radio Technology AB. From 2005 to 2006, he was with ScandiNova Systems AB, Uppsala. From 2006 to 2011, he was Postdoctoral Researcher with the Space Research Institute, Austrian Academy of Sciences, Graz, Austria. From 2008 to 2011, he was a Senior Lecturer with the Department of Physics and Astronomy, Uppsala University. From 2012 to 2023, he was with ScandiNova Systems AB, which produces pulse modulators and complete RF units, which outputs high-power microwaves. At ScandiNova Systems AB, he was responsible for RF, including design and test of both low-level and high-power klystron and magnetron RF-systems, including complete customized waveguide systems, both pressurized and for ultra-high vacuum. Since 2018, he has been a Senior Researcher with the Department of Electrical Engineering, Division of Solid-State Electronic, Microwave in Medical Engineering Group, Uppsala University, where he is involved in research and teaching. His main research interests include microwave engineering and antennas.

Robin Augustine graduated in Electronics Science from Mahatma Gandhi University, India, in 2003. He received master's degree in Electronics with Robotics specialization from Cochin University of Science and Technology, India, in 2005. Received Doctoral degree in Electronics and Optic Systems from Univerisité Paris Est Marne La Vallée, France, in July 2009. He is author or co-author of more than 230 publications including journals and conferences and has three patents. He is Associate Professor at Uppsala University in Medical leading the Microwaves in Medical Engineering Group (MMG). He has pioneered the Fat-Intrabody Communication technique, Recipient of Swedish research agency, Vetenskapsrådet's (VR) project grant 2017 and 2023 for his projects on A Novel Modality for Osteodiagnosis and Musculoskeletal Diagnosis, respectively. He is Co-PI of several EU projects. He is partnering in the SSF 2022 grant Body Centric Operating System – BOS. He is currently coordinating EU Horizon 2020 FET-OPEN Science Excellence project B-CRATOS, a visionary project in man–machine interface.